Journal of
Synchrotron
Radiation

ISSN 1600-5775

Received 3 May 2013
Accepted 6 September 2013

High-resolution thermal imaging with a combination of nano-focus X-ray diffraction and ultra-fast chip calorimetry

Martin Rosenthal,[a]‡ David Doblas,[b,c]‡ Jaime J. Hernandez,[b] Yaroslav I. Odarchenko,[b] Manfred Burghammer,[d] Emanuela Di Cola,[d] Denis Spitzer,[c] A. E. Antipov,[a] L. S. Aldoshin[a] and Dimitri A. Ivanov[a,b]*

[a]Faculty of Fundamental Physical and Chemical Engineering, Moscow State University, Moscow 119991, Russian Federation, [b]Institut de Sciences des Matériaux de Mulhouse, CNRS UMR7361, CNRS, 15 rue Jean Starcky, Mulhouse 68057, France, [c]Institut Franco–Allemand de Recherches de Saint-Louis, Laboratoire des Nanomatériaux pour les Systèmes Sous Sollicitations Extrêmes, UMR3208, ISL/CNRS, 5 Rue du Général Cassagnou, Saint-Louis 68301, France, and [d]European Synchrotron Radiation Facility, 6 rue Jules Horowitz, Grenoble 38043, France.
*E-mail: dimitri.ivanov@uha.fr

A microelectromechanical-systems-based calorimeter designed for use on a synchrotron nano-focused X-ray beamline is described. This instrument allows quantitative DC and AC calorimetric measurements over a broad range of heating/cooling rates ($\leq$100000 K s^{-1}) and temperature modulation frequencies ($\leq$1 kHz). The calorimeter was used for high-resolution thermal imaging of nanogram-sized samples subjected to X-ray-induced heating. For a 46 ng indium particle, the measured temperature rise reaches $\sim$0.2 K, and is directly correlated to the X-ray absorption. Thermal imaging can be useful for studies of heterogeneous materials exhibiting physical and/or chemical transformations. Moreover, the technique can be extended to three-dimensional thermal nanotomography.

Keywords: nanocalorimetry; modulated differential scanning calorimetry; micro-focus X-ray diffraction; indium.

1. Introduction

The generation of heat during X-ray beam materials irradiation has found applications ranging from single-photon detection for X-ray spectroscopy (McCammon *et al.*, 1984) to non-invasive thermal imaging for identification of beam damage (Snell *et al.*, 2007). X-ray-induced heating has also been used for creation and diagnosis of a solid-density plasma (Vinko *et al.*, 2012) and for controlled decomposition of the energetic materials (Beard, 1991). Generally, it is clear that the evaluation of the X-ray-induced heat can provide material-specific information because the interaction cross sections of the X-ray photons, such as those due to photoelectric, Rayleigh and Compton contributions, depend on the atomic number and sample mass density. Previously, several studies [*cf.* Snell *et al.* (2007), and references therein] focused on the quantitative evaluation of beam-induced temperature rise. In particular, computations were performed for the case of a typical biocrystal sample exposed to fluxes of third-generation synchrotron radiation sources operated at photon energies typical for the crystallographic work (12 keV). It was found that the temperature rise in samples generally stays small, varying from a fraction of a degree to a couple of degrees, which is explained by the low total X-ray beam power (1–4 mW) and low density of organic materials. Because of the small rise in the temperature of such samples, measurement of X-ray-beam-induced heating employing conventional non-invasive thermal imaging is challenging. Here, we show that the use of advanced microelectromechanical systems (MEMS)-based nanocalorimeters in combination with nano-focused X-ray beams (Minakov *et al.*, 2005*a*) helps to alleviate this problem and allows thermal mapping of extremely small samples (1–100 ng in weight) with micrometre spatial resolution. It is noteworthy that nano-focused X-ray beams have recently proved to be very helpful in elucidating the local-scale structure of semicrystalline polymers (Rosenthal *et al.*, 2011, 2012).

MEMS-based calorimetric sensors capable of performing quantitative thermo-analytical measurements on extremely small samples were first introduced in the 1990s by L. Allen

‡ These authors contributed equally to this work.

(Allen *et al.*, 1994). One of the first commercially available MEMS sensors produced by the Xensor company (TCG 3880) reached a sensitivity of 1 nJ K^{-1} and a time resolution of 5 ms (Minakov *et al.*, 2005*b*). The approaches toward quantitative nanocalorimetric experiments were developed further by M. Merzlyakov (Merzlyakov, 2006) and C. Schick (Minakov & Schick, 2007). In our group, an electronic interface for a nanocalorimeter was built which is compatible with different types of commercial calorimetric sensors and allows operation in both DC and AC modes (Piazzon *et al.*, 2010). The instrument is capable of conducting quantitative DC and AC calorimetric measurements over a broad range of heating/cooling rates ($\leq$100000 K s^{-1}) and temperature modulation frequencies ($\leq$1 kHz). Despite the existence of commercial chip calorimeters such as Flash DSC from Mettler Toledo, our own nanocalorimeter was specially designed to simplify synchrotron measurements; the measuring cell of the Flash DSC instrument is fixed directly on top of the electronic interface which prevents any *in situ* combination of calorimetric measurements with X-ray diffraction in transmission. Moreover, commercial instruments do not support AC calorimetric measurements, which is crucial for compatibility with a relatively slow technique like X-ray diffraction. In general, the open design of our nanocalorimeter makes the combination of our system with other physical characterization techniques rather straightforward (Piazzon, 2010).

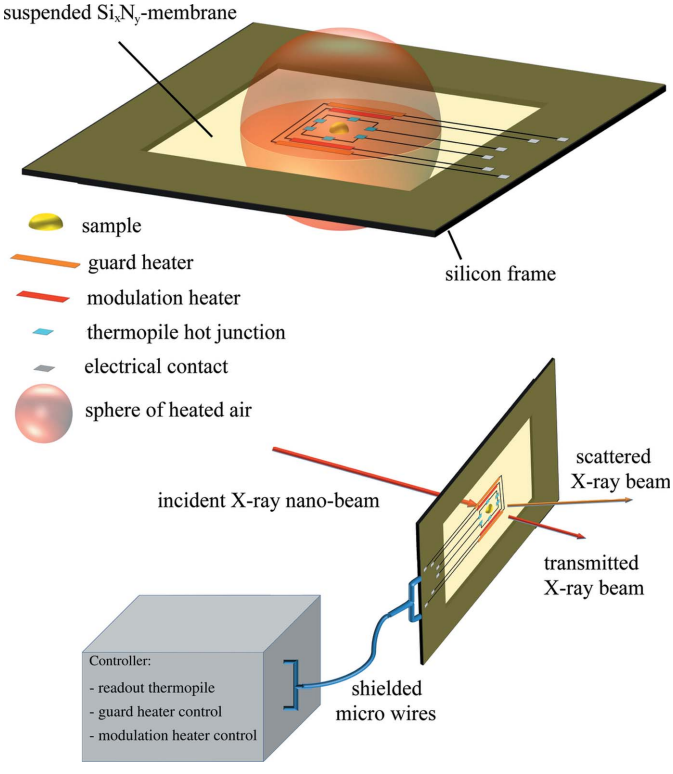

Figure 1
Schematics of the nanocalorimeter set-up used for *in situ* nano-focus X-ray beam measurements. The nanocalorimeter sensor (top) consists of a silicon frame with a thin suspended silicon nitride membrane on which are assembled two pairs of electric heaters (the so-called modulator and guard heaters) as well as six thermopiles connected in series. The calorimetric experiments are realised with the help of a custom-built electronic controller.

2. Experimental

A schematic of the experimental set-up used in this study is shown in Fig. 1. The *in situ* calorimetric measurements were performed with the help of a MEMS-type sensor consisting of a thin suspended silicon nitride membrane with assembled electric heaters and thermopiles (*cf.* Fig. 1, top). The guard heater was used for linear heating and cooling ramps, whereas the modulation heater allowed for temperature modulation experiments. In the course of the measurements, the heaters generate a small sphere of heated air around them, which facilitates heat exchange with the sample deposited on the membrane. The calorimetric experiments are enabled by an electronic interface, which applies the programmed voltage pulses to the heaters and allows for fast thermopile readout.

The nano-beam X-ray diffraction measurements were carried out at the ID13 beamline [*cf.* Fig. 1 (bottom) and Fig. 2(*a*)] of the European Synchrotron Radiation Facility (ESRF; Grenoble, France). A flat Si-based nanocalorimetric MEMS-type sensor is mounted on a perforated flat ceramic plate (Fig. 2*b*) allowing for X-ray measurements in transmis-

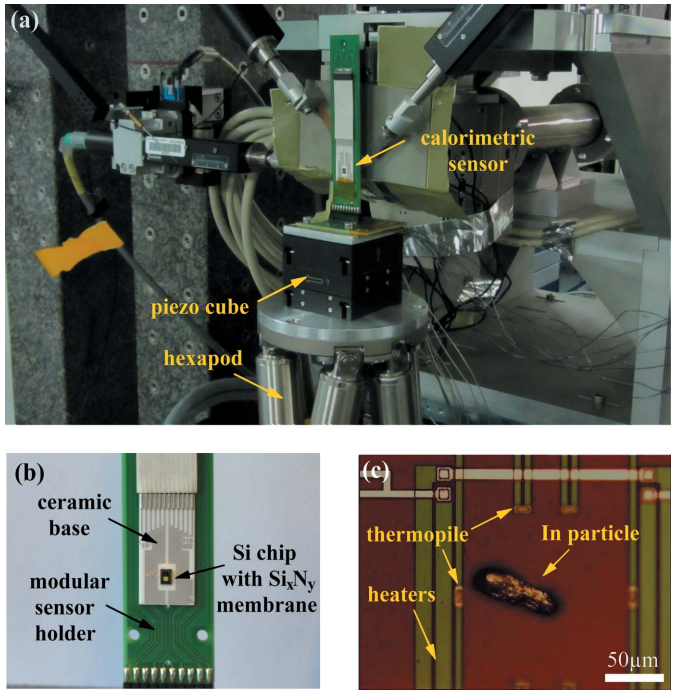

Figure 2
(*a*) View of the sample stage at the ID13 nano-hutch facility at the ESRF with the nanocalorimetric sensor holder installed. The sensor is positioned vertically on top of a piezo-actuator (black cube) to allow the scanning of the region of interest with nanometre resolution. (*b*) Closer view of the custom-made modular sensor holder. The nanocalorimetric sensor is mounted onto a flat ceramic base compatible with X-ray diffraction in transmission. (*c*) A micrometre-sized In particle placed within the active area of the nanocalorimetric sensor. The heating elements and hot junctions of the thermopile are in close vicinity of the particle.

sion. The Si_xN_y membrane of the XEN-39392/XEN-40014 sensor employed has a lateral size of 900 μm × 900 μm and is only 1 μm thick; it is therefore practically transparent for the X-ray beam. Two pairs of resistive heating elements and six differential thermopiles connected in series constitute the active area of 100 μm × 100 μm (Fig. 2*c*). The low heat conductivity and low heat capacity of the Si_xN_y membrane are crucial in reaching the required sensitivity to nanogram-sized samples. For the X-ray absorption and nano-diffraction experiments, X-ray photons with an energy of 14.92 keV were used. The final footprint of the beam on the sample of about 150 nm × 150 nm was achieved using nano-focusing refractive X-ray lenses with a focal distance of 14 mm (Boye *et al.*, 2009). The size of the beam is the main parameter defining the spatial resolution of the nano-beam X-ray diffraction measurement. The two-dimensional diffraction patterns were collected using a two-dimensional Frelon N4 camera with 50 μm × 50 μm pixels. The norm of the scattering vector s [$s = 2\sin(\theta)/\lambda$] was calibrated using several reflections of corundum. The X-ray absorption data were recorded using an X-ray-sensitive diode placed 60 cm downstream of the sample. The absorption data signal was corrected for absorption of the X-ray beam in the air and in the bare silicon nitride membrane.

In this study, *in situ* nano-focus X-ray diffraction combined with MEMS-based nanocalorimetry was performed on a single micrometre-sized indium particle (Strem Chemicals, purity 99.999%). This material was selected for thermal imaging due to its high absorption (mass attenuation coefficient μ/ρ of $\sim$44.45 cm^2 g^{-1} at 15 keV) and its well known thermodynamic parameters; it is conventionally used as a thermal calibrant for differential scanning calorimetry (DSC). During the measurements, the sensor was operated exclusively in the AC mode, where a small current (current amplitude 0.1 mA, current offset 0.3 mA) oscillating at a frequency of $\sim$40 Hz is applied to the heating elements while performing experiments at constant heating rates or in quasi-isothermal conditions (Minakov *et al.*, 2005*a*). This operation mode is similar to the conventional modulated DSC technique (Jiang *et al.*, 2002). In this mode, the sample is subjected to heating power oscillations while its temperature response is measured. In our case, by passing a small oscillating current through the heating elements we generate thermal power, which results in small periodic temperature oscillations making it possible to measure the sample heat capacity (Kraftmakher, 2002).

3. Discussion

For the thermal imaging, a microparticle of In was positioned within the active area of the calorimetric sensor with the help of a micromanipulator (Fig. 2*c*). During the experiment it was visualized with a slide-in on-axis optical microscope in reflection. The particle was exposed to either 2 s or 20 s of pulsed incident X-ray radiation (Fig. 3*a*, top). The calorimeter measured an increase of about 0.2 K, closely following the sequence of the X-ray beam exposures (Fig. 3*a*, middle). Importantly, the measured temperature increase is independent of the X-ray pulse length. In this case, the power provided by the X-ray beam exposure becomes very rapidly compensated by the heat losses through the atmosphere, as will be described later in the text. The rate at which the thermal equilibrium is reached is comparable with the characteristic time of the calorimetric sensor, which equals approximately 4 ms. Therefore the temperature rise (*cf.* Fig. 3*b*) rarely shows any middle points; the latter can appear only accidentally, due to a slightly asynchronized data acquisition. For both temperature values (*i.e.* with and without the X-ray beam switched on) the noise levels are comparable; thus, for the sequence of 20 s pulses they equal 7.8 and 8.3 mK, respectively. Importantly, the amplitude of the temperature modulation ($T_{\rm mod}$) exhibits no visible change in these conditions (Fig. 3*a*, bottom).

The analysis of the $T_{\rm mod}$ values can be performed with a simple model employed for interpretation of the modulated DSC data (Jiang *et al.*, 2002; Kraftmakher, 2002). It is assumed that the oscillating power with amplitude P is consumed heating the sensor with a loaded sample having the total heat capacity at constant pressure $C_{\rm p,sample} + C_{\rm p,membrane}$, as well as for the heat exchange with the atmosphere characterized by the power exchange coefficient Q (Piazzon *et al.*, 2010; Kraftmakher, 2002),

$$T_{\rm mod} = \frac{P}{\left\{\left[\left(C_{\rm p,membrane} + C_{\rm p,sample}\right)\omega\right]^2 + Q^2\right\}^{1/2}}, \qquad (1)$$

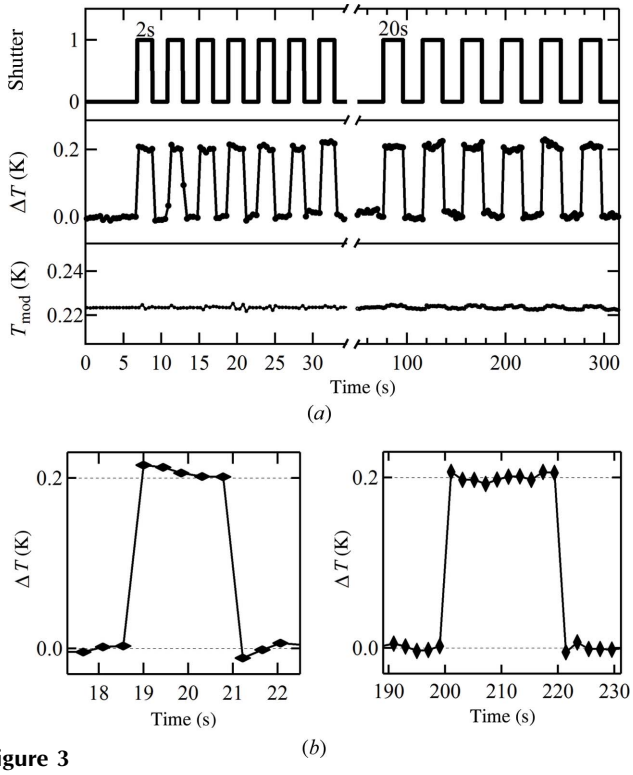

Figure 3
(*a*) Room-temperature experiment showing the heating effect of a nano-focused X-ray beam modulated by a sequence of fast-shutter openings (top). Variation of the In particle temperature (middle) and temperature modulation amplitude (bottom). (*b*) Zoomed segments of the temperature profile due to individual X-ray pulses of 2 and 20 s (left and right, respectively).

where Q is the proportionality coefficient between the applied power and the temperature rise of the sensor. The constancy of T_{mod} during the experiment shows that, under these conditions, *i.e.* far away from the phase transitions, the sample heat capacity is not affected by the incident X-ray beam. Moreover, by comparing the T_{mod} values measured for the unloaded and loaded sensor and by using the experimental heat exchange coefficient Q (59.0 μW K^{-1}), $C_{p,sample}$ was calculated to be 12.9 nJ K^{-1}. This corresponds to a sample weight of 56 ng.

In Fig. 4(*a*), a two-dimensional map of the In particle was generated with a 2 μm lateral resolution using the scattered intensity of a single 110 crystalline reflection of In (*cf.* inset of Fig. 4*a*). The spatial distribution of the scattering intensity nicely reproduces the particle shape, as observed optically (*cf.* Fig. 2*c*). This unambiguously shows that the particle has a single-crystalline nature. Fig. 4(*b*) shows the spatially resolved X-ray absorption for the same particle.

The classical expression for the intensity of transmitted light is

$$I_x = I_0 \exp[-(\mu/\rho)\rho x], \qquad (2)$$

where I_0 is the incident beam intensity, I_x is the intensity of the transmitted beam after passing through a slab of material of thickness x, ρ is the mass density of the material and μ/ρ is the mass attenuation coefficient. When the absorption $A = (I_0 - I_x)/I_0$ is known, the local thickness of the particle can be derived from equation (2) (*cf.* Fig. 4*c*). The resulting thickness map permits the calculation of the total volume and mass of the particle, which equal 6350 μm^3 and 46 ng, respectively. The latter value is in reasonable agreement with the one computed previously from equation (1).

By measuring the sample temperature rise (ΔT) due to absorption of the nano-focused X-ray beam, the temperature distribution map of the particle was generated (*cf.* Fig. 4*d*). It can be seen that the thermal image reproduces the shape of the particle. If one assumes full conversion of the absorbed photon energy to heat followed by rapid thermal equilibration, the ΔT value can be expressed as follows,

$$\Delta T = \frac{(I_0 - I_x)U}{Q\Delta t} \quad \text{or} \quad \Delta T = \frac{W_{beam}}{Q}A. \qquad (3)$$

In equation (3), U is the energy of one photon, Δt is the beam exposure time excluding the detector read-out time and W_{beam} is the X-ray beam power (29.2 μW).

To validate the hypothesis underlying equation (3), the ΔT values were correlated to the local X-ray absorption. For the sake of clarity, the comparison is firstly given for one cross section of the respective maps in Fig. 4(*e*), showing good correspondence between them. Then, the statistic correlation is displayed for all data points in Fig. 4(*f*). From the last figure, it can be concluded that there is indeed a linear correlation of the sample temperature rise to the spatially resolved absorption. Moreover, the slope of the linear fit shown on the graph (0.53) is reasonably close to the expected value of 0.49 [*cf.* equation (3)]. The standard deviation of the temperature residual gives the upper bound for the temperature noise (15 mK), which after conversion to power gives the instrument power sensitivity of 900 nW.

Fig. 5 displays the results of simultaneous nanocalorimetric and X-ray diffraction experiments performed on the same In particle either during heating and cooling ramps at a constant heating rate or during quasi-isothermal measurements. Thus, the one-dimensional-reduced WAXS diffractograms recorded as a function of temperature distinctly show the onset of melting/crystallization transitions occurring at 430.0 ± 0.75 and 429 ± 0.75 K, respectively (see Fig. 5*a*). This shows that the developed nanocalorimetric accessory can be conveniently used as a normal heating stage for nano-focus X-ray diffraction. Moreover, the melting transition of In is clearly visible on

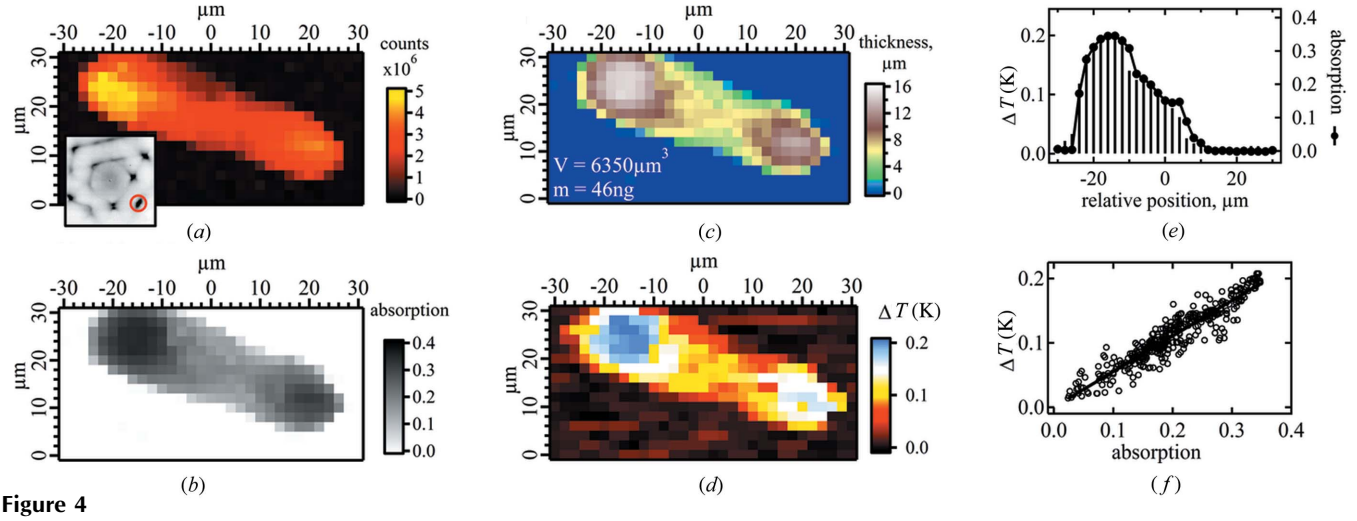

Figure 4
(*a*) Image of the same In particle as in Fig. 2(*c*) obtained by mapping the intensity of a selected 110 reflection of In (encircled on the two-dimensional WAXS pattern in the inset). The pixel size is 2 μm × 2 μm. (*b*) Image of the particle obtained using absorption of the incident X-ray beam. (*c*) Topographical map of the particle recalculated from the absorption image given in (*b*). (*d*) Rise of the particle temperature due to the incident X-ray beam plotted as a function of the spatial position. (*e*) The horizontal cross section of the temperature map in (*d*) is given as vertical sticks and that of the X-ray absorption in (*b*) shown as filled circles. Both cross sections correspond to the line y = 25 μm. (*f*) Increase of the In particle temperature as a function of the X-ray beam absorption for the whole scanned area. The solid line is the linear fit to the data.

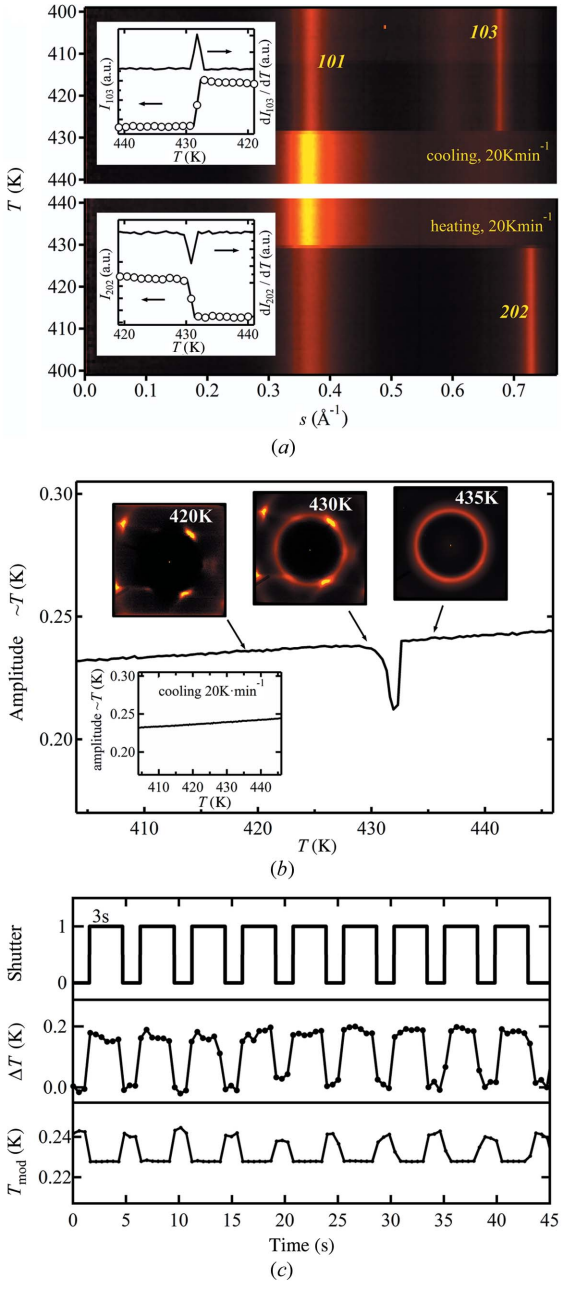

Figure 5
(*a*) One-dimensional-reduced WAXS curves measured in the temperature range from 400 to 440 K at a rate of 20 K min^{-1}. The insets show diffraction intensities and their first derivatives for the 202 reflection (heating ramp) and 103 reflection (cooling ramp). (*b*) Amplitude of the temperature modulation recorded simultaneously with X-ray diffraction for the heating ramp. The inset gives the curve corresponding to cooling and two-dimensional WAXS patterns measured at different temperatures. (*c*) Quasi-isothermal experiment at 430 K showing the heating effect of a fast-shutter-modulated X-ray beam (top). The resulting variation of the particle temperature and modulation amplitude is shown in the middle and bottom panels, respectively.

the calorimetric temperature-modulation curve in Fig. 5(*b*), where it is identified as a negative peak. The decrease of $T_{\rm mod}$ in this region corresponds to an increase in the complex heat capacity of the sample in the melting region [*cf.* equation (1)], which is a typical observation in the modulated DSC experiments (Jiang *et al.*, 2002).

After the sample is completely molten, the modulation amplitude increases again. The selected two-dimensional WAXS diffractograms given on the same figure panel show that the initially highly crystalline sample (T = 420 K) starts to display a mixture of crystalline reflections and amorphous halo at 430 K, before becoming completely molten at 433 K. The observed co-existence of crystalline and amorphous fractions in the diffractograms of In recorded over a finite temperature range is not usual since this material melts and crystallizes very rapidly. Such co-existence can only be accounted for by repeated melting/recrystallization events occurring during thermal modulation cycles whose peak-to-peak amplitude is, in this case, approximately 0.4 K. Since the rate of the WAXS detector recording is much slower than the modulation frequency applied, the CCD camera receives a time-averaged view of the sample state. Interestingly, the modulated cooling curve does not reveal the crystallization transition, although it is safely detected by X-rays. The latter fact can be explained by the high rate of this process, whose characteristic time is much smaller than the duration of one cycle.

The heating effect of the X-ray beam measured at the verge of melting (Fig. 5*c*) is similar to the one at room temperature (*cf.* Fig. 3*a*). However, the amplitude modulation signal shows a qualitatively different behaviour. Thus, in this case the fast-shutter openings are accompanied by a noticeable decrease of $T_{\rm mod}$. This can be explained by the fact that heating of the sample with the X-ray beam brings it further into the melting region, where $T_{\rm mod}$ is reduced for the reasons explained before. Thus, the dynamic thermal response of the sample (*i.e.* $T_{\rm mod}$) measured in quasi-isothermal conditions during X-ray beam exposures can provide additional information on the phase transitions occurring in the sample.

4. Conclusions

In summary, we report on a newly designed ultra-fast MEMS-based calorimeter accessory for synchrotron nano-focused X-ray diffraction. The instrument allows quantitative DC and AC calorimetric measurements in a broad range of heating/cooling rates ($\leq$100000 K s^{-1}) and temperature modulation frequencies ($\leq$1 kHz). Here we performed quantitative thermal imaging of a nanogram-sized metal sample exposed to an X-ray beam. We show that the resulting temperature rise is correlated with spatially resolved X-ray absorption. In the future, similar thermal imaging can be extended to organic materials such as single bio-crystals, which, as mentioned in §1, also show temperature rise upon irradiation with X-rays. However, in this case, special care will be required to minimize beam-induced degradation.

For the case of inert homogeneous materials such as microparticles of In, the thermal mapping provides information similar to thickness images. However, the thermal imaging at elevated temperature, which combines measurements of the static temperature rise and temperature modulation amplitude, can provide information on the sample thermal behaviour. One can imagine that the temperature

signal can be collected simultaneously with X-ray absorption during the standard nanotomography experiments. We expect that thermal imaging in three dimensions (thermal nanotomography) can help guide studies of heterogeneous materials exhibiting physical (*e.g.* phase transitions) and chemical (*e.g.* curing reactions) transformations at different temperatures.

DD acknowledges the PhD bursary granted by the EADS Foundation. The authors thank the financial support provided by IUPAC, project PAC-PAL-10-02-26, and by the Russian Ministry of Science and Education (grants 11.G34.31.0055 and 14.518.11.7013). The authors are particularly grateful to A. I. Bondar for the design of the instrument and to Professor G. E. Ice for valuable advice in preparing this manuscript. MR is grateful to Stefan Rosenthal for the support in the technical development of the sensor stage.

References

Allen, L. H., Ramanath, G., Lai, S. L., Ma, Z., Lee, S., Allman, D. D. J. & Fuchs, K. P. (1994). *Appl. Phys. Lett.* **64**, 417.
Beard, B. C. (1991). *Propel. Explos. Pyrotech.* **16**, 81–87.
Boye, P., Feldkamp, J. M., Patommel, J., Schwab, A., Stephan, S., Hoppe, R., Schroer, C. G., Burghammer, M., Riekel, C., van der Hart, A. & Küchler, M. (2009). *J. Phys. Conf. Ser.* **186**, 012063.
Jiang, Z., Imrie, C. T. & Hutchinson, J. M. (2002). *Thermochim. Acta*, **387**, 75–93.
Kraftmakher, Y. (2002). *Phys. Rep.* **356**, 1–117.
McCammon, D., Moseley, S. H., Mather, J. C. & Mushotzky, R. F. (1984). *J. Appl. Phys.* **56**, 1263.
Merzlyakov, M. (2006). *Thermochim. Acta*, **442**, 52–60.
Minakov, A., Adamovsky, S. & Schick, C. (2005*b*). *Thermochim. Acta*, **432**, 177–185.
Minakov, A. A., Roy, S. B., Bugoslavsky, Y. V. & Cohen, L. F. (2005*a*). *Rev. Sci. Instrum.* **76**, 043906.
Minakov, A. A. & Schick, C. (2007). *Rev. Sci. Instrum.* **78**, 073902.
Piazzon, N. (2010). PhD thesis, Université de Haute Alsace, Mulhouse, France.
Piazzon, N., Rosenthal, M., Bondar, A., Spitzer, D. & Ivanov, D. (2010). *J. Phys. Chem. Solids*, **71**, 114–118.
Rosenthal, M., Bar, G., Burghammer, M. & Ivanov, D. A. (2011). *Angew. Chem. Int. Ed.* **50**, 8881–8885.
Rosenthal, M., Portale, G., Burghammer, M., Bar, G., Samulski, E. T. & Ivanov, D. A. (2012). *Macromolecules*, **45**, 7454–7460.
Snell, E. H., Bellamy, H. D., Rosenbaum, G. & van der Woerd, M. J. (2007). *J. Synchrotron Rad.* **14**, 109–115.
Vinko, S. M. *et al.* (2012). *Nature (London)*, **482**, 59–62.